New Concept for Electrically Driven Air Compressors for Commercial Vehicles—General Layout and Indicator Measurements

Max Joswig, Konrad Klotsche, Thomas Mösch, Jörg Nickl, and Christiane Thomas

Abstract The shift from fossil-fueled internal combustion engines to electrically powered vehicles leads to further electrification of many sub-systems. However, in commercial vehicles, systems powered by compressed air will prevail. This leads to a demand for mobile electrically driven air compressors. They require a compact and lightweight design as well as oil-free and high-speed operation. A careful and thorough development process is crucial to meet the challenging requirements. For example, the examination and understanding of the process within the working chambers using indicator measurements are valuable in providing information on key performance indicators (e.g., indicated work, valve behavior and energy efficiency). In this paper, two topics are presented: First, the fundamental compressor layout of the two-stage four-cylinder reciprocating compressor and its unique characteristics are shown. The unconventional design results in outstanding compactness while ensuring the required mass force balancing and throughput. Second, indicator measurements and specific features of their evaluation are presented. In particular, it is shown how to solve the problem of impaired crank angle detection using logarithmic indicator diagrams.

Keywords Mobile reciprocating air compressor · Electrically driven compressor · Commercial vehicle · Oil-free · Pneumatic energy system

1 Introduction

Commercial vehicles are usually equipped with pneumatically operated braking systems. Compressed air generates the braking force; thus braking does not depend on the force of the driver's foot. An air compressor in the vehicle delivers compressed

M. Joswig (✉) · K. Klotsche · T. Mösch · J. Nickl · C. Thomas
Bitzer-Chair of Refrigeration, Cryogenics and Compressor Technology, Technische Universität Dresden, Dresden, Germany
e-mail: max.joswig@tu-dresden.de

ambient air [1]. Additionally, several other sub-systems depend on this compressed air system, too (e.g., tilting of the vehicle, adjustment of the driver seat).

The shift towards electrically powered commercial vehicles leads to challenging requirements for the air compressor: The characteristics of an electric motor that replaces the previous mechanical drive need special consideration. Furthermore, the absence of harsh noise and vibrations from the combustion engine also results in other noise sources becoming more prominent. Low energy consumption of the vehicle requires an energy-efficient, compact, and lightweight compressor. On top of that, new specifications sometimes require oil-free operation; thus the compressor must operate without oil. The high discharge pressure and the demanding volume flow remain unchanged compared to previous applications.

Fitzgerald and Jiang [2] developed a screw compressor for commercial vehicles. Contrary to the oil-free requirement, it features oil injection for increased energy efficiency and lower discharge temperatures. The publication claims that higher reliability and lower maintenance costs than reciprocating compressors have been achieved. It is also shown that a screw compressor could be a suitable choice even if comparably small airflows and high-pressure ratios are needed.

However, literature is scarce on current developments of other types of compressors for electrically powered commercial vehicles. Nonetheless, this paper presents a prototype-stage reciprocating compressor featuring oil-free operation comprising the basic compressor layout, mass force balancing and indicator measurements.

2 Compressor Layout

The developed compressor prototype features a two-stage operation able to reach discharge pressures up to low double-digit bar pressures. The cylinders are arranged to a very compact layout, as seen in Fig. 1a: The cylinders of each stage are combined on a joint cylinder bank to form a V90-machine. The first-stage cylinders of larger diameter flank the smaller second-stage cylinders.
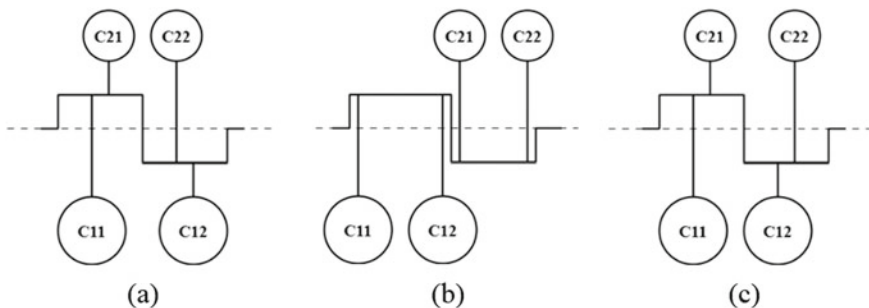
Fig. 1 Compressor layout of the investigated compressor prototype (**a**) and of conventional layouts (**b**, **c**)

The arrangement of the two second-stage cylinders in between the first-stage cylinders makes use of the present space and avoids adding further crank length to accommodate the second-stage cranks, as in Fig. 1b and c. In this paper, the two first-stage cylinders refer to C11 and C12, and the second-stage cylinders refer to C21 and C22.

The offset angle of the two crank pins is 180°. One cylinder of each stage shares a crank pin. The top dead centers (TDC) of each cylinder follow the sequence: C11–C21–C22–C12: 0°–270°–90°–180°.

The crank pin offset and the oscillating masses m_s in kg (piston, piston pin, oscillating part of the piston rod), lead to a favorable mass force balancing. The mass forces $F_{m,osc}$ (in N) are calculated by the crankpin radius r (in m), the angular velocity ω (in rad/s), and the dimensionless pushrod ratio λ as a function of the crankpin position α (in rad):

$$F_{m,osc} = m_s \cdot r \cdot \omega^2 \cdot (\cos\alpha + \lambda \cdot \cos 2\alpha) \tag{1}$$

whereas the pushrod ratio represents the quotient of crankpin radius r and length of the piston rod l (in m):

$$\lambda = \frac{r}{l}. \tag{2}$$

A balance of mass moments of the counter-rotating forces (marked with - in index) calculates through the acting counter-rotating mass forces and their respective levers. The hereby-considered moment balance is depicted in Fig. 2 on the center of gravity R of the crankshaft. The levers of each acting mass forces are named a and b. They represent a half of the cylinder bore distance of the first-stage and second-stage cylinders, respectively.

The oscillating mass forces are depicted in relation to their maximum in Fig. 3a as a function of the crank angle. The crank angle position of 0° refers to the TDC of C11. Figure 3b shows the mass moments resulting from the counter-rotating mass forces turning around the center of gravity of the crankshaft.

Fig. 2 Mass force and moment balance around center of gravity of crankshaft
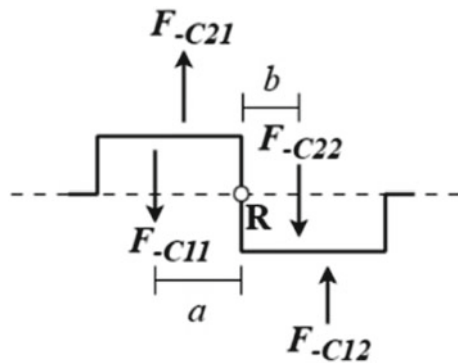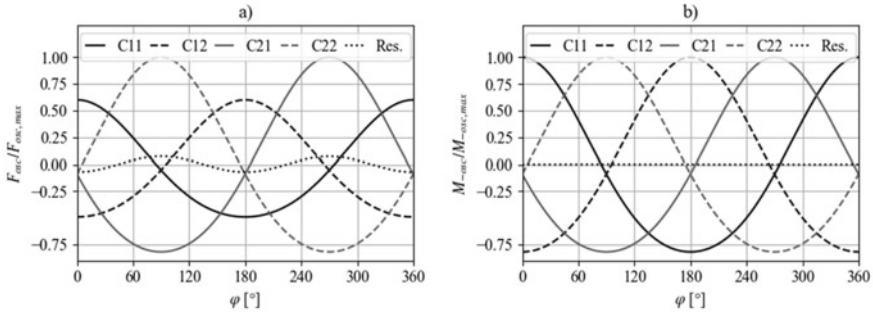
Fig. 3 Oscillating mass forces (**a**) and mass moments of counter-rotating mass forces (**b**)

The force balance in Fig. 2 shows that the mass forces of the cylinders within a stage act contrary due to the crank angle offset of 180°. Nevertheless, the mass forces are not entirely compensated. However, the mass moments of the counter-rotating mass forces are perfectly balanced. This is due to the chosen mass ratio of the first and second-stage cylinders as depicted in the balance of moment in Eq. (3):

$$F_{-m,osc,C11/12} \cdot a = F_{-m,osc,C21/22} \cdot b \tag{3}$$

The mass of the second-stage cylinders is deliberately raised according to the ratio of the cylinder bore distances. This results in a perfect balancing of mass moments due to counter-rotating mass forces while slightly increasing the amplitude of the oscillating mass forces. Despite that, the increase is a result of the twice as fast turning part of the oscillating mass force depicted in Eq. (1). The effect is further mitigated through a small push rod ratio λ.

The combined arrangement of the second-stage cylinders in the presented compressor layout leads to an overall shorter axial length of the compressor. The result is an outstandingly compact compressor while maintaining similar mass force balancing compared to conventional layouts.

3 Experimental Methodology for Indicator Measurements

3.1 Instrumentation

An indicator measurement to analyze the processes within the working chambers of the compressor prototype was performed. High-frequency sensors within all four working chambers (referred to as WC) and additionally in each suction and discharge chamber of the first and second stages synchronously recorded the pressure over time.

These pressure sensors feature a small and robust body design to fit in the compression chambers and to withstand high temperatures. Furthermore, a photoelectric

Table 1 Sensors for the experimental investigation

Parameter	Location	Sensor type	Measurement range	Uncertainty
p	WC11 + WC12	Kulite XCE-062	0–7 bar (a)	± 0.1% FSO
p	WC21 + WC22 + discharge 2nd	Kulite XTEL-190LM	0–17 bar (a)	± 0.1% FSO
p	Suction 1st	Kulite XTM-190S (M)	0–3.5 bar (a)	± 1.0% FSO
p	Discharge 1st + suction 2nd	Kulite IS-XTEL-375 M	0–17 bar (a)	± 0.1% FSO
TDC	Shaft	ifm OGP200		

Table 2 Experimental plan

	2000 rpm	2400 rpm	2800 rpm
10 bar	Pressures WC11 + WC12 + WC21 + WC22		
13 bar	Pressures discharge + suction chambers: 1st + 2nd stage		

sensor was fitted to the compressor to determine the top dead center (TDC). Temperature sensors were added near the pressure transducers for calibration purposes. Table 1 contains a list of the used sensors.

Each pressure was recorded synchronously at a sampling rate of 100 kHz using a National Instruments high-speed data acquisition device. The experimental plan includes different operation points regarding the compressor discharge pressure and rotational speed. For the compressor discharge pressure, $p_D = 10$ bar and $p_D = 13$ bar have been investigated. The rotational speed of the compressor ranges from 2000 to 2800 rpm. The operational points and the measured parameters are shown in Table 2.

3.2 Crank Angle Error Analysis

The measured data include pressures of each cylinder and pressures of the common suction and discharge chambers of the first and second stages. The sensor of crank angle experienced a failure and could not be substituted. Therefore, no helpful crank angle data is available.

The TDC of C21 was estimated from the measured pressure data: The theoretical number of samples for each rotation provides an approximate time frame for the periodicity of the pressure signal. The crank angle span from 0° to 360° is evenly distributed over the estimated periodicity. The other TDCs can be calculated using the known angle offsets. The following analysis includes data from one crank revolution.

The methodology is subject to errors due to the ambiguous TDC location. The number of samples within an actual periodicity can vary, and the true TDC might also be located between two sample points. Furthermore, a flawed assignment of the

change of the chamber volume to the measured pressures due to ambiguous time data leads to the considered error in further data analysis.

An illustrative plot of data is given in Fig. 4a. It shows the indicator diagram of the first cylinder of the second stage. The volume change is shown relative to the stroke, including the dead volume of the cylinder. The pressure is represented in relation to the suction pressure of the working chamber. The data shows the actual pressure change for the estimated TDC. The resulting plots of a crank angle error of $\pm 2°$ are also shown. Finally, the ideal indicator diagram is presented based on the assumption of adiabatic compression of dry air, with a heat capacity ratio of $\gamma = 1.4$ for compression and $\gamma = 1.2$ for expansion [3], and an ideal valve behavior during suction and discharge. Figure 4b shows the same functions within a logarithmic indicator diagram.

A negative error leans the curves away from the enclosed area of the work cycle. The logarithmic depiction underlines that: The curves bend away right after the BDC and TDC. This effect is evident in the logarithmic depiction as the compression and expansion curves become more bulbous.

The positive crank angle error shrinks the enclosed area. The compression curve starting from the BDC and the expansion curve starting from the TDC lean into the enclosed area.

It is important to note that other effects overlay the described effects. For instance, a leaking suction valve would also flatten the compression curve but also make the expansion curve steeper. A leaking discharge valve would cause the opposite effect.

The effects are further discussed in the literature, e.g. by Machu [4] and Kim and Soedel [5]. They subjected their work to further analysis of crank angle errors and came to similar conclusions to the observations in this paper. Therefore, it can be assumed that the estimated TDC in this paper is within a range of $\pm 2°$ of crank angle error, since the typical effects of the error can already be seen in this range.
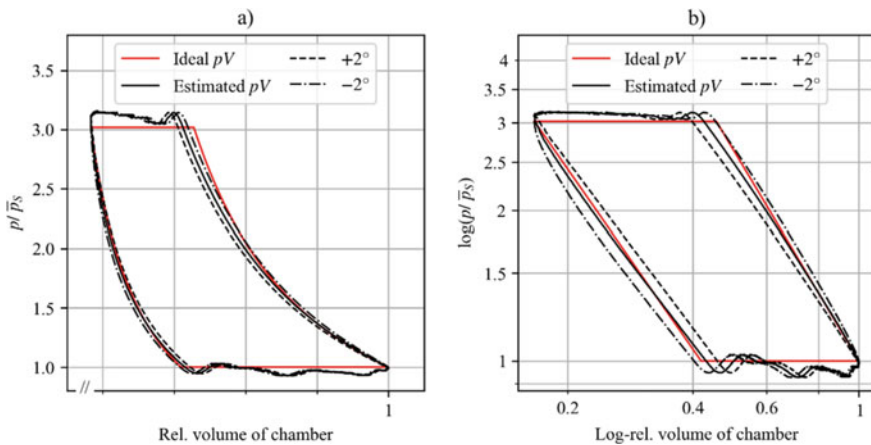
Fig. 4 Indicator diagram (**a**) and logarithmic indicator diagram (**b**)

3.3 Indicated Work and Loss Analysis

The indicated work represents the work transferred from the piston to the gas in every cycle. The amount equals the area within the measured curve $f = p(V)$ and is highlighted in Fig. 5. The indicated work W_{Ind} (in J) can be determined by Eq. (4):

$$W_{Ind} = \left| -\oint p(V)dV \right|. \tag{4}$$

The ideal indicated work enclosed by the adiabatic compression and expansion without suction and discharge losses shown in Fig. 4 is presented relative to the indicated work and is calculated by Eq. (5):

$$W_{Ind,ideal} = \left| -\oint p_{ideal}(V)dV \right|. \tag{5}$$

The indicated isentropic efficiency is then calculated by Eq. (6):
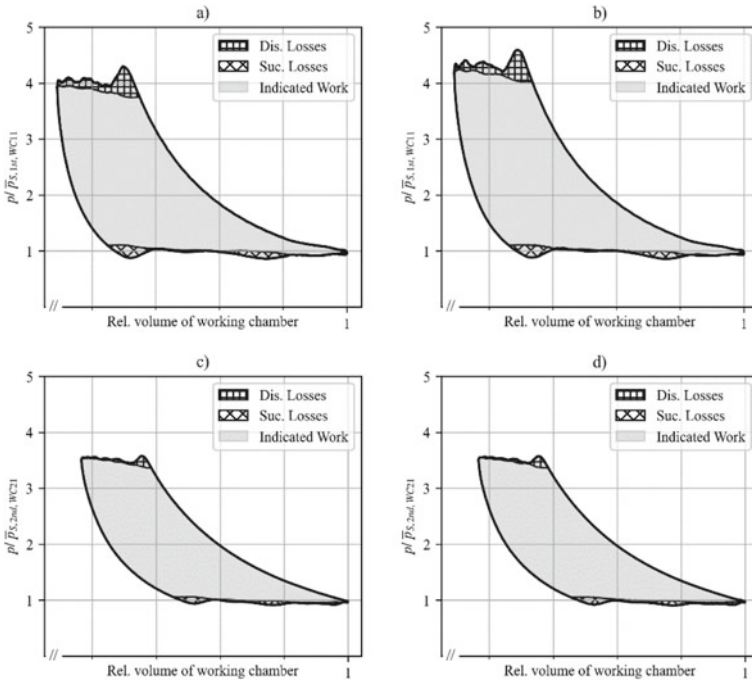
Fig. 5 Indicator diagrams for WC11 for $p_D = 10$ bar and $n = 2000$ rpm (**a**), for $p_D = 13$ bar, $n = 2000$ rpm (**b**), WC21 for $p_D = 10$ bar and $n = 2000$ rpm (**c**) and for $p_D = 13$ bar and $n = 2000$ rpm (**d**)

$$\eta_i = \frac{W_{Ind,is}}{W_{Ind}}. \tag{6}$$

Suction pressure losses occur during the period of an open suction valve as the gas flows through the valve. The work equals the area enclosed between the pressure level of the suction and the working chamber during intake marked with cross hatches on Fig. 5. The additional effort (in J) caused by the suction pressure losses can be calculated using Eq. (7):

$$W_{loss,suc} = \int_{V_{beg,suc}}^{V_{end,suc}} p_{suc}(V)dV - \int_{V_{beg,suc}}^{V_{end,suc}} p(V)dV. \tag{7}$$

Discharge pressure losses occur when the discharge valve opens, and the gas exits the working chamber through the valve into the discharge chamber. The loss equals the area enclosed between the pressure in the working chamber and the discharge chamber during discharge. The area is marked with hatch patterns on Fig. 5 and the additional effort (in J) can be calculated using Eq. (8):

$$W_{loss,dis} = \int_{V_{beg,dis}}^{V_{end,dis}} p(V)dV - \int_{V_{beg,dis}}^{V_{end,dis}} p_{dis}(V)dV. \tag{8}$$

Eventually, the pressure ratio of the stages is calculated using Eq. (9):

$$\pi = \frac{\frac{1}{n} \sum_1^n p_{dis}(V)}{\frac{1}{n} \sum_1^n p_{suc}(V)} \tag{9}$$

4   Results and Discussion

4.1   Indicator Diagrams

Figure 5 provides the indicator diagrams of the two stages (WC11 + WC21) of the operational point at $p_D = 10$ bar and $n = 2000$ rpm in (a) and (c) and of the operational point $p_D = 13$ bar and $n = 2000$ rpm in (b) and (d).

The diagrams show the influence of the different compressor discharge pressures. It can be seen on Fig. 6, that the increase of compressor pressure ratio increases the pressure ratio of both stages. However, an increased stage pressure ratio and the larger relative dead volume of the second stage flattens the expansion curve since more compressed mass in the dead volume needs to expand. Thus, the pV-diagrams with a discharge pressure of 13 bar in Fig. 5b and d appear slightly narrower than the diagrams (a) and (c) for a compressor discharge pressure of 10 bar.

Fig. 6 Pressure ratios of WC11 and WC21
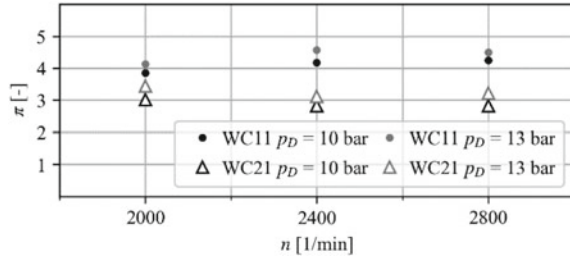
4.2 Suction and Discharge Pressure Losses

Figure 7 depicts the suction and discharge pressure losses for each cylinder and stage. The results include the losses relative to the indicated work of each cylinder.

The losses increase with higher rotational speed. The suction pressure losses for the first-stage cylinders in Fig. 7a increase from 3.0% at 2000 rpm to 5.0% at 2800 rpm. The discharge pressure losses in Fig. 7b range from roughly 4.0 to 5.0%. There only minor difference with varying compressor discharge pressure.

The suction pressure losses of the second stage shown in Fig. 7c increase with an increase in the rotational speed from 1.8% at 2000 rpm to 5.0% at 2800 rpm. The discharge pressure losses shown in Fig. 7d range from 1.5 to 2.5% for $p_D = 13$ bar, followed by the $p_D = 10$ bar ranging from 1.8 to 3.5%. The increased discharge pressure losses with lower discharge pressures could be due to increased mass flow as the suction process begins earlier. Furthermore, higher speeds increase the mass flow that needs to pass the discharge chamber and could also lead to higher losses during intake and discharge.

4.3 Indicated Isentropic Efficiency

Figure 8a shows the indicated isentropic efficiency of the first-stage cylinders. The efficiency decreases for higher rotational speeds from 102% (2000 rpm) to 86–92% (2800 rpm). Higher losses for suction and discharge (as seen in Fig. 7) contribute to this observation.

The efficiencies in Fig. 8b for the second stage change from 95% (2000 rpm), 99–105% (2400 rpm) to 98–106% (2800 rpm). A significant change with higher rotating speeds and different compressor discharge pressure cannot be seen.

A difference in indicated work at different compressor discharge pressures cannot be reliably detected within the error range. However, an increased compressor discharge pressure does not necessarily lead to a higher indicated work. It can be seen in Fig. 5 that an increased pressure ratio flattens the expansion curves. Thus, less gas that needs to be compressed enters the cylinder. Ultimately, the throughput of the compressor decreases.
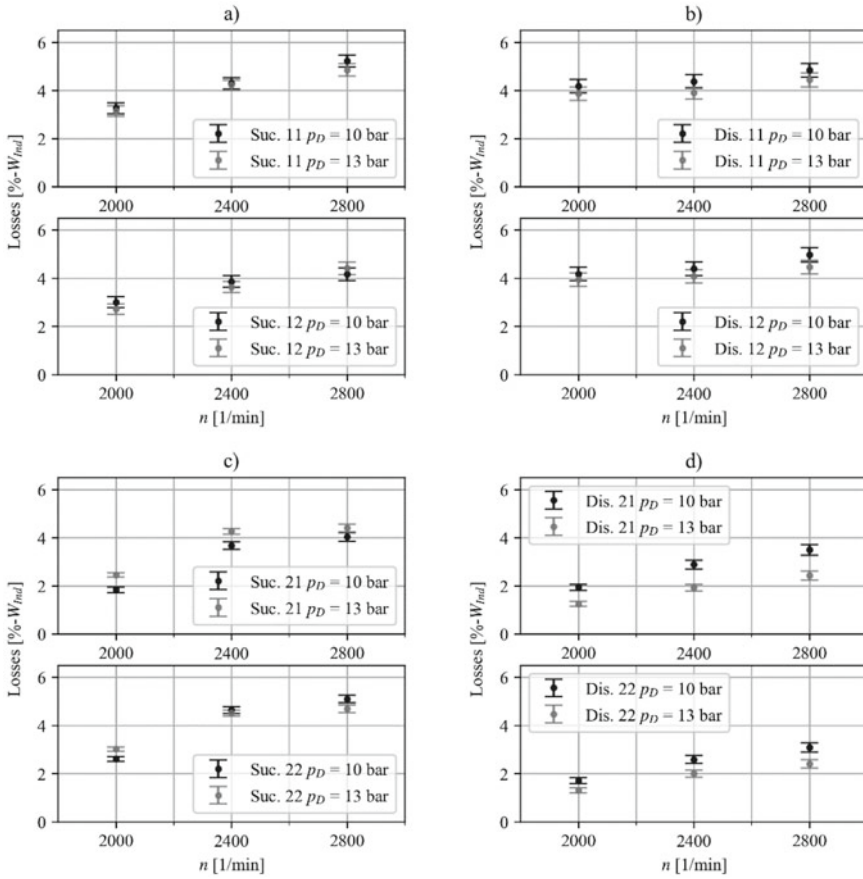
Fig. 7 Suction losses 1st stage (**a**), discharge losses 1st stage (**b**), suction losses 2nd stage (**c**) and discharge losses 2nd stage (**d**) relative to indicated work

It should be noted that the indicated isentropic efficiencies over 100% are possible due to the compressor operation. The active cylinder cooling removes compression heat and pushes the present polytropic compression process away from isentropic towards isothermal compression. This results in a flatter compression curve compared to the isentropic compression, as can be seen in Fig. 4a. The ideal isentropic compression work needed can surpass the indicated work due to removed heat. Eventually, through the definition of isentropic efficiency in Eq. (6), values larger than 100% can be a result.
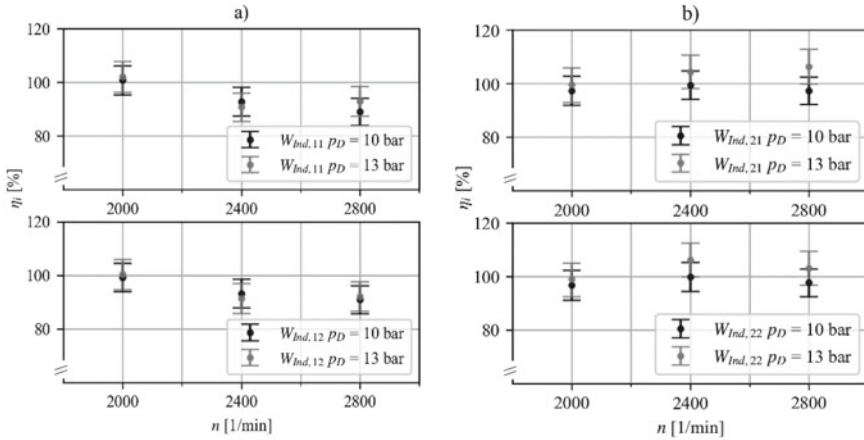
Fig. 8 Indicated isentropic efficiency work for both cylinders of the 1st stage (**a**) and the 2nd stage (**b**)

5 Conclusions

The paper presents a prototype-stage electrically driven reciprocating air compressor for commercial vehicles in terms of its fundamental layout and the results of an indicator measurement.

The unique design characteristics result in a compact design and beneficial mass balance.

The evaluation of the pressure measurements shows outstanding suction and discharge pressure losses and compression efficiencies. Furthermore, the unexpected failure of the crank angle measurement could be compensated by varying the assumed TDC position and subsequently evaluating the corresponding logarithmic indicator diagrams. Further investigations to improve the operating behavior of the prototype will focus on determining further efficiencies and leakages.

References

1. W. Appel, H. Brähler, S. Breuer, *Nutzfahrzeugtechnik: Grundlagen, Systeme, Komponenten*, 7th edn. (Vieweg+Teubner, Wiesbaden, 2013)
2. B. Fitzgerald, B. Jiang, Development of a rotary screw compressor for electric truck air brake and suspension system. SAE Int. J. Commer. Veh. **14**(3), 421–427 (2021)
3. M.I. Frenkel, *Kolbenverdichter - Theorie, Konstruktion und Projektierung* (VEB Verlag Technik, Berlin, 1969)
4. E.H. Machu, Reciprocating compressor diagnostics detecting abnormal conditions from measured indicator cards, in *International Compressor Engineering Conference*, Paper 1155 (Purdue University, 1996)
5. J. Kim, W. Soedel, On experimental errors in P-V diagrams, in *International Compressor Engineering Conference*, Paper 563 (Purdue University, 1986)